Chemosphere 270 (2021) 128651

Contents lists available at ScienceDirect

Chemosphere

journal homepage: www.elsevier.com/locate/chemosphere

Photocatalytic degradation of tetracycline antibiotics using delafossite silver ferrite-based Z-scheme photocatalyst: Pathways and mechanism insight

Jiayin Guo [a, b, 1], Longbo Jiang [a, b, 1], Jie Liang [a, b, *], Weihua Xu [a, b], Hanbo Yu [a, b], Jin Zhang [a, b], Shujing Ye [a, b], Wenle Xing [a, b], Xingzhong Yuan [a, b]

[a] College of Environmental Science and Engineering, Hunan University, Changsha, 410082, PR China
[b] Key Laboratory of Environment Biology and Pollution Control, Hunan University, Ministry of Education, Changsha, 410082, PR China

HIGHLIGHTS

- 20-BAF possesses enhanced photocatalytic activity for tetracycline degradation.
- Ag^0 exhibits SPR effect for enhanced light absorption and acts as Z-scheme bridge.
- Tetracycline was degraded into small organic compounds or entirely mineralized.
- The smooth transfer of interface charges follows the Z-scheme pathway.

GRAPHICAL ABSTRACT

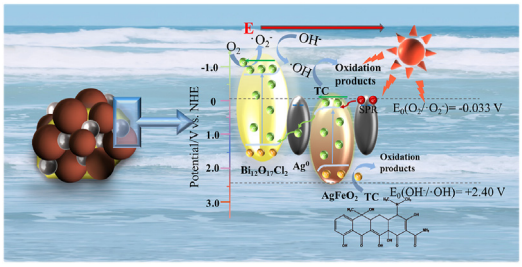

ARTICLE INFO

Article history:
Received 10 July 2020
Received in revised form
12 October 2020
Accepted 15 October 2020
Available online 21 October 2020

Handling Editor: E. Brillas

Keywords:
Tetracycline degradation
Photocatalysis
$Bi_{12}O_{17}Cl_2$/Ag/$AgFeO_2$
Z-Scheme

ABSTRACT

Tetracycline (TC), a widely used antibiotic, is easy to enter the aquatic ecosystem through soil erosion, livestock manure and wastewater discharge, resulting in a series of risks. The application of Z-scheme photocatalysts with efficient interface charge separation and transfer has been regard as an effective strategy for antibiotic degradation. Herein, a novel ternary Z-scheme $Bi_{12}O_{17}Cl_2$/Ag/$AgFeO_2$ was successfully synthesized by ultrasound-assisted ethanol reduction of Ag^+ on the interface of $Bi_{12}O_{17}Cl_2$ and $AgFeO_2$. The $Bi_{12}O_{17}Cl_2$/Ag/$AgFeO_2$ Z-scheme system exhibited an enhanced photocatalytic degradation capability for TC, which was over 6.5 times and 2.4 times higher than those of $AgFeO_2$ and $Bi_{12}O_{17}Cl_2$/$AgFeO_2$ system, respectively. The photocatalytic process of TC was explored, and the results indicated that an optimum catalyst concentration of 0.5 g L^{-1} and a primeval pH (without adjustment) favored the degradation process, while the introduction of exogenous anions (CO_3^{2-}, SO_4^{2-} and NO_3^-) and organic matter (HA) supressed the degradation of TC. Simultaneously, the possible pathway for the degradation process of TC was presented based on the liquid chromatography-mass spectrometry (LC-MS) analysis. Active species trapping experiments and ESR spectra revealed the significant contribution of $^{\bullet}O_2^-$ in the TC degradation, and verified the Z-scheme mechanism of the $Bi_{12}O_{17}Cl_2$/Ag/$AgFeO_2$ system.

1. Introduction

Tetracycline ($C_{22}H_{24}N_2O_8$, TC), a typical antibiotic, has been widely applied in agriculture, animal husbandry and

* Corresponding author. College of Environmental Science and Engineering, Hunan University, Changsha, 410082, PR China.
E-mail addresses: liangjie82@163.com, liangjie@hnu.edu.cn (J. Liang).
[1] Co-first author

https://doi.org/10.1016/j.chemosphere.2020.128651
0045-6535/

pharmaceutical industry (Wang et al., 2011). The resulting abuse of TC causes a large amount of residues to enter the aquatic ecosystem via the soil erosion, animal manure and wastewater effluent, leading to a range of risks, such as the selection of resistant bacteria, affecting the structure and activity of the microbial populations (Zhang et al., 2015; Wang et al., 2018a). However, tetracyclines is difficult to be removed by traditional wastewater treatment technology (prechlorination, biological treatment, adsorption, membrane filtration, etc.) due to its stable molecular structure and poor biodegradability (Kumar Ray et al., 2019; Wang et al., 2019; Ye et al., 2019; Xing et al., 2020). Therefore, finding an effective way to remove tetracyclines from the aqueous environment is crucial. Recently, photocatalysis has been considered as a promising and sustainable candidate for pollutant removal because it can degrade and even mineralize contaminants into harmless CO_2 and H_2O with the simple aid of solar energy (Jiang et al., 2018; Wang et al., 2018b; Yu et al., 2019; Sun et al., 2020). Especially, Z-scheme photocatalytic system has aroused great interest because it not only possess the ability of swift photo-generated electrons and holes separation, but also retain prominent redox capacity (Huang et al., 2019; Zeng et al., 2019). Besides, in many Z-scheme systems, the noble metal (Pt, Au, Ag, etc) played a tremendous part. For example, Bu et al. prepared Z-Scheme Ag_3PO_4/Ag/WO_{3-x} photocatalyst by in situ reduction method (Bu et al., 2015). Ag nanoparticles serving as carrier-transfer centers effectively improve the photocatalytic degradation performance of Z-Scheme Ag_3PO_4/Ag/WO_{3-x} system. Furthermore, our previous research demonstrated that the effective electrons transfer together with SPR effect of Ag nanoparticles bring the enhancement of photocatalytic performance of Z-scheme Ag_2CO_3/Ag/WO_3 (Yuan et al., 2017).

Delafossite oxide $AgMO_2$ (M = Fe, Co, Ni, Cr) have attracted much attention owing to their excellent electronic structure (Song and He, 2017). Among them, silver ferrite ($AgFeO_2$) is easily excited to yield photo-generated carriers under visible-light illumination due to its narrow bandgap (Ouyang et al., 2009; Tang and Zhang, 2017a). Furthermore, its merits of non-toxic and biocompatibility make $AgFeO_2$ a rising star in the field of photocatalysis. Yin et al. (2016) firstly applied $AgFeO_2$ to methyl orange photodegradation with 97% removal rate after 180 min visible light exposure (Yin et al., 2016). Then, Kashyap et al. (2018) realized the 99.6% removal of 2,4,6-trichlorophenol by polypyrrole/$AgFeO_2$ photocatalyst under visible light with the aid of ultrasonic bath (Kashyap and Riaz, 2018). Many researchers were devoted to improving the photocatalytic performance of $AgFeO_2$. However, up to now, the photocatalytic performance of $AgFeO_2$ without external energy is still limited by easy agglomeration, poor sunlight utilization, swift electron-hole pairs recombination and slow carriers transfer. Furthermore, it is found that the Ag^+ in $AgFeO_2$ can easily be reduced to Ag (Tang and Zhang, 2017b). Generally, the formation of Ag nanoparticles on the surface of semiconductor is beneficial for the photocatalytic performance due to its surface plasmon resonance effect which can remarkably enhance the light harvesting ability and its electron conductivity which can facilitate the separation of photoexcited electron-hole pairs (Guo et al., 2018). Therefore, we believed that it is a promising strategy to construct an Ag/$AgFeO_2$ based Z-scheme system to obtain excellent photocatalytic effect.

$Bi_{12}O_{17}Cl_2$ has the potential to form all-solid-state semiconductor-metal-semiconductor Z-scheme system with $AgFeO_2$ via the connection of Ag nanoparticles, due to their suitable band structures. In addition, the flaky morphology of $Bi_{12}O_{17}Cl_2$ is conducive to the dispersion of $AgFeO_2$ particles, which is considered to be an ideal substrate (Zhou et al., 2018b; Wang et al., 2020b). Lately, $Bi_{12}O_{17}Cl_2$ has aroused a great deal of interest in applying to environmental remediation, due to its excellent photophysical, chemical properties, nontoxicity and stability (Zhou et al., 2018a, 2018b). Thus, there are enough reasons to believe that $Bi_{12}O_{17}Cl_2$ is an excellent candidate for improving the photocatalytic performance of $AgFeO_2$.

In this work, a novel ternary $Bi_{12}O_{17}Cl_2$/Ag/$AgFeO_2$ (BAF) Z-Scheme heterostructure was synthesized for photodegradation of TC under visible light illumination. Additionally, various characterizations were applied to systematically explore the chemical composition, morphology, optical and photoelectrochemical properties of the as-prepared photocatalysts. Furthermore, the potential impacts of environmental factors on the photocatalytic degradation of TC was evaluated. Importantly, the TC photodegradation pathway and the internal mechanism of 20-BAF for enhancing photocatalytic activity was also analyzed.

2. Experiment section

2.1. Chemicals and materials

$Bi(NO_3)_3 \cdot 5H_2O$, NH_4Cl, $AgNO_3$, $Fe(NO_3)_3 \cdot 9H_2O$, NaOH, ethanol and ethylene glycol (EG) were purchased from Sinopharm Chemical Reagent Corp, P. R. China. Ultrapure (UP) water (18.25 MΩ cm^{-1}) was used during the experimental process, obtained from Millipore system. All chemicals were analytical grade and used without further purification.

2.2. Synthesis of the photocatalyst

The $Bi_{12}O_{17}Cl_2$/$AgFeO_2$ (BF) was prepared by an in-situ deposition-precipitation method (Tang and Zhang, 2017a). Specifically, a certain amount (19.6, 29.4, 39.2 and 49 mg) of the previously synthesized $Bi_{12}O_{17}Cl_2$ (BOC, the detailed synthesis process was shown in Supporting Information) was added to 15 mL of UP water and ultrasonically dispersed for 0.5 h. Thereafter, 1 mmol $Fe(NO_3)_3 \cdot 9H_2O$ and 1 mmol $AgNO_3$ were successively added to above $Bi_{12}O_{17}Cl_2$ solution and stir for 30 min. Then, 5 mL of NaOH solution (1.6 M) was added dropwise to the above suspension at the rate of 1 mL min^{-1} and stir for another 5 h. Subsequently, the precipitate was collected by centrifugation, washed three times with UP water, and dried at 60 °C overnight. The samples were denoted as 10-BF, 15-BF, 20-BF and 25-BF when the mass ratio of added $Bi_{12}O_{17}Cl_2$ and $AgFeO_2$ precipitated were 10%, 15%, 20% and 25%, respectively. Besides, we determined the Bi content in the as-prepared products by ICP-OES. It was calculated that the actual contents of BOC in 10-BF, 15-BF, 20-BF and 25-BF were 8.6%,12.3%,15.8%,19.1% respectively. The pure $AgFeO_2$ (AFO) was fabricated by the similar process without the addition of $Bi_{12}O_{17}Cl_2$.

$Bi_{12}O_{17}Cl_2$/Ag/$AgFeO_2$ (BAF) composite was fabricated by an ultrasound (US)-assisted ethanol reduction method. Ultrasound is a simple and fast method to reduce Ag^+ to Ag^0 (Eq. (4)) (Anandan and Ashokkumar, 2009). The ·OH and ·H radicals formed in water vapor under ultrasound exposure are active species for application of reduction and oxidation (Eq. (1)) (Tang and Zhang, 2017b). Besides, the addition of ethanol can consume oxidation radicals and promote the formation of reduction radicals (Eqs. (2) and (3)) (Tang and Zhang, 2017b). Firstly, the as-prepared BF precipitation was collected and transferred into a 50 mL beaker with 30 mL of absolute ethanol solution in it. The beaker was placed in an ultrasonication instrument (JP-020S, China) with an input power of 120 W at frequency of 40 kHz for 2 min. Finally, the precipitation was washed, dried and collected. Subsequently, the resultant precipitate was centrifuged and dried at 60 °C overnight in an oven. A series of $Bi_{12}O_{17}Cl_2$/Ag/$AgFeO_2$ samples were synthesized by changing the types of BF, which were denoted as 10-BAF, 15-BAF, 20-BAF and 25-BAF when the BF added in ethanol were 10-BF, 15-

BF, 20-BF and 25-BF respectively. Meanwhile, the Ag/$AgFeO_2$ (AF) composite was prepared by the similar method without the presence of $Bi_{12}O_{17}Cl_2$.

$$H_2O(US) \rightarrow \cdot H + \cdot OH \quad (1)$$

$$CH_3CH_2OH + \cdot OH \rightarrow CH_3\dot{C}HOH + H_2O \quad (2)$$

$$CH_3CH_2OH(US) \rightarrow \text{pyrolysis radicals} \quad (3)$$

$$Ag\,(I) + \text{reduction radicals}\,(\cdot H + CH_3\dot{C}HOH + \text{pyrolysis radicals}) \rightarrow Ag^0 \quad (4)$$

2.3. Experimental process and characterization

The detailed experimental operation of photocatalytic activity analysis, cycle experiment, degradation pathways analysis, and reactive species trapping experiments as well as characterization method were exhibited in Supporting Information.

3. Results and discussion

3.1. Characteristics of the photocatalyst

3.1.1. Composition and morphology analysis

The XRD analysis results (Fig. 1) exhibited the crystallinity and purity of the synthesized photocatalyst. The characteristic peaks of AFO at 2θ = 14.27°, 28.78°, 43.78°, 50.52°, 60.89° and 68.77° could be clearly observed in BAF samples which indexed to (0 0 2), (0 0 4), (0 0 6), (1 0 5), (1 1 0) and (1 1 4) crystal planes, respectively. Besides, the diffraction peaks of BOC samples were inapparent in BF composite and BAF samples. Only diffraction peaks at 2θ = 29.20°, 32.88° corresponded to lattice plane (117) and (200) could be found, which might be owing to the low content of BOC and the full cladding by AFO. The presence of BOC could be also confirmed by the results of XPS. In addition, the peaks of AFO in BF and BAF samples obviously became weaker and broader, indicating that the introduction of $Bi_{12}O_{17}Cl_2$ led to a decrease in crystallinity. No impurity peaks were seen in the XRD patterns. Furthermore, as displayed in Fig. 1b, clear peaks at around 38.1° and 44.3° could be observed in 20-BAF, while they were absent in 20-BF, proving the formation of cubic Ag^0 (JCPDS 04–0783) during the ultrasonic treatment.

The surface elemental compositions and chemical states was measured by the X-ray photoelectron spectrum (XPS). As shown in Fig. 2a, the total survey XPS spectra of 20-BAF confirmed the presence of major elements Ag, Fe, O, Bi and Cl, which was consistent with the results of XRD and EDS. Fig. 2b showed the Ag 3d spectrum of AFO and 20-BAF in high resolution. Both AFO and 20-BAF contained two peaks at approximately 367.4 and 373.4 eV which were assigned to the binding energies of Ag $3d_{5/2}$ and Ag $3d_{3/2}$ of Ag (I) in $AgFeO_2$. Moreover, the 374.1 and 368.0 eV could be attributed to Ag^0 on the interface between AFO and BOC (Tang and Zhang, 2017b). According to the analysis of the peak area ratio of Fig. 2b, the ratio of Ag^+ to Ag^0 was estimated to be 20:1. While, no peaks ascribed to Ag^0 was observed in AFO. The bands at 723.8 and 710.8 eV in Fig. 2c were ascribed to Fe $2p_{1/2}$ and Fe $2p_{3/2}$ peaks, which were accompanied by a satellite peak at 717.8 eV, demonstrating the existence of Fe^{3+} species in the catalysts (Yamashita and Hayes, 2008). In Fig. 2d, the peaks at 163.7 and 158.4 eV refer to Bi $4f_{5/2}$ and Bi $4f_{7/2}$, respectively, which indicated the existence of Bi^{3+} species in 20-BAF (Zhou et al., 2018a). Besides, compared with pure BOC, reduction of peaks intensity occurs over 20-BAF, which indicated that the low content of BOC in 20-BAF. As for Cl 2p (Fig. 2e), its spectrum contained two distinct peaks at 198.9 and 197.3 eV, ascribing to Cl $2p_{1/2}$ and Cl $2p_{3/2}$ of Cl^- ions in 20-BAF samples, respectively (Zhou et al., 2018b). Furthermore, the offset of binding energy of Ag, Fe, Bi and Cl in 20-BAF (Fig. 2b–e) further confirmed that the combination between AFO and BOC affected the electronic energy distribution (Greiner et al., 2011). Specifically, the binding energies of Bi and Cl exhibited negative movements in 20-BAF, while Ag and Fe showed positive shifts. The results further illustrated the existence of a strong interaction between AFO and BOC. Besides, the binding energy in XPS has negative correlation with surface electron density, so these shifts reveal that electrons migrate from AFO to BOC, which attribute to the formation of Z-scheme heterojunction between AFO and BOC interface (Li et al., 2020).

The morphology and compositions of AFO, BOC, and 20-BAF were measured by SEM with the energy-dispersive spectrometry (EDS) analysis (Fig. SM-1). Fig. SM-1a demonstrated that pure AFO composed of spherical-like particles and exhibited serious aggregation due to their high surface energy and the nature of $AgFeO_2$ delafossite (El-Bassuony and Abdelsalam, 2018). The agglomeration led to a decrease of reactive sites, which is unfavorable to the photodegradation of TC. Due to its laminar atomic structures, $Bi_{12}O_{17}Cl_2$ underwent self-hydrolysis, nucleation, and oriented growth to form nanosheets, which were then assembled into large

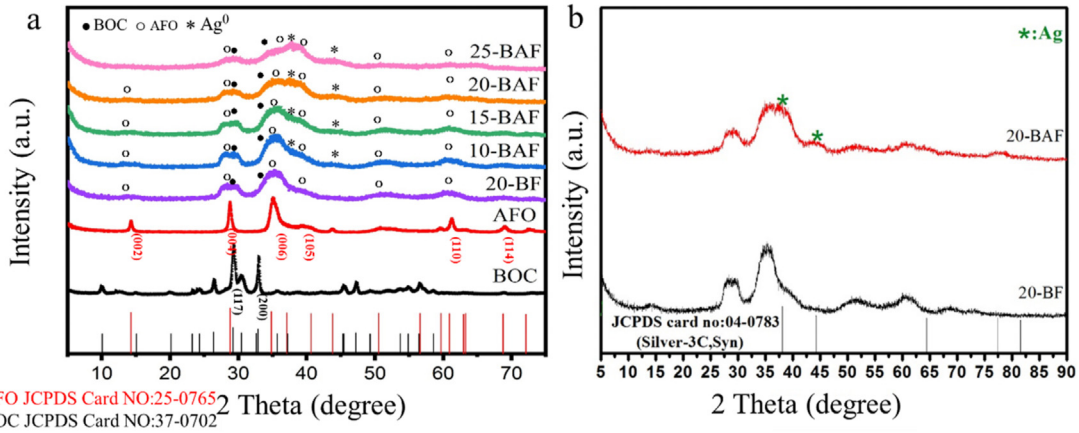

Fig. 1. (a) XRD patterns of pristine $AgFeO_2$, $Bi_{12}O_{17}Cl_2$, $Bi_{12}O_{17}C_{12}/AgFeO_2$ and $Bi_{12}O_{17}Cl_2/Ag/AgFeO_2$ composites and (b) XRD comparison chart of 20-BAF and 20-BF.

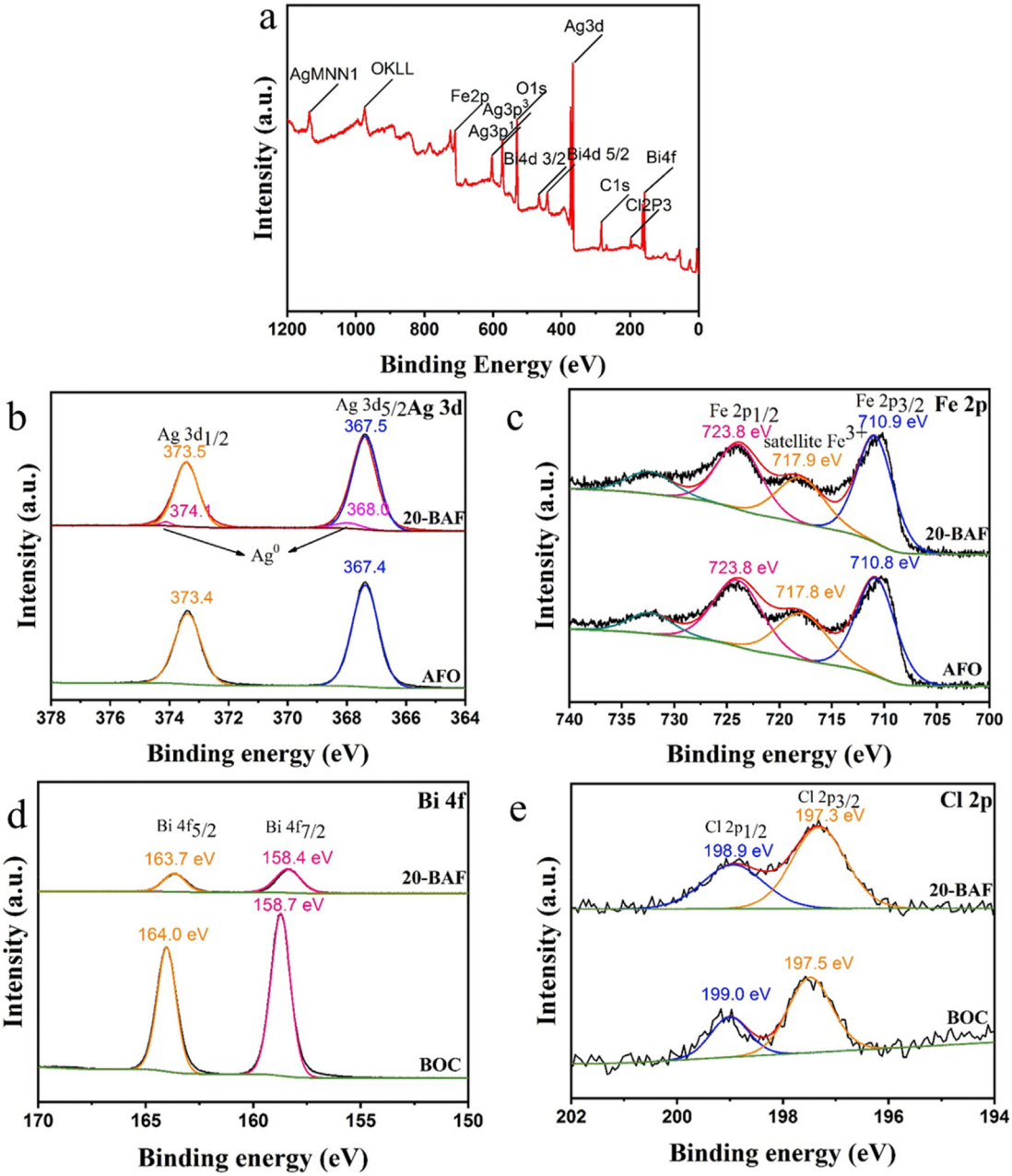

Fig. 2. XPS spectra: (a) survey scan of 20-BAF sample and high-resolution scan of (b) Ag 3d, (c) Fe 2p, (d) Bi 4f and (e) Cl 2p.

clusters in a plane-to-plane manner, as displayed in Fig. SM-1b (Chang et al., 2015). It is obvious that 20-BAF composites were composed of irregular clusters formed by loading AFO particles on BOC nanosheets skeleton (Fig. SM-1c). Meanwhile, the elemental mappings (Fig. SM-1d–h) informed that Ag, Fe, O, Bi and Cl elements evenly distributed on 20-BAF. The TEM graphics (Fig. 3) further confirmed that AFO appears as spherical nanoparticles, while BOC was stacked nanosheets. Besides, it was easy to observe that the introduction of BOC mitigated the agglomeration of AFO (Fig. 3c). Furthermore, the HRTEM image shown in Fig. 3d exhibited that the lattice fringes spacing of AFO is 0.242 nm, corresponding to the (102) crystallographic plane, suggesting that there was no change in the lattice structure of AFO after the appearance of BOC and Ag^0. Also, the observed lattice fringes of 0.306 and 0.235 nm matched well with (117) facet of BOC and (111) facet of Ag^0. Based on the above analysis, metallic Ag and AFO were successfully loaded on the surface of BOC to form BAF photocatalysts by the present facile strategy.

3.1.2. Optical and electrochemical properties

UV–vis DRS with the wavelength range of 200–800 nm was adopted to measure the optical absorption properties of AF, 20-BF, 20-BAF composites along with pure AFO and BOC. As exhibited in Fig. 4a, the absorption edges of pure BOC and pure AFO were located at about 520 nm and 750 nm, respectively. As for 20-BF and AF, the absorption ability in 600 nm–800 nm region was slightly enhanced. After the formation of Z-scheme, it could be observed that the absorption ability of 20-BAF in 600 nm–800 nm region was improved significantly when compared with AFO, and the absorption range of 20-BAF was extended to the entire visible light

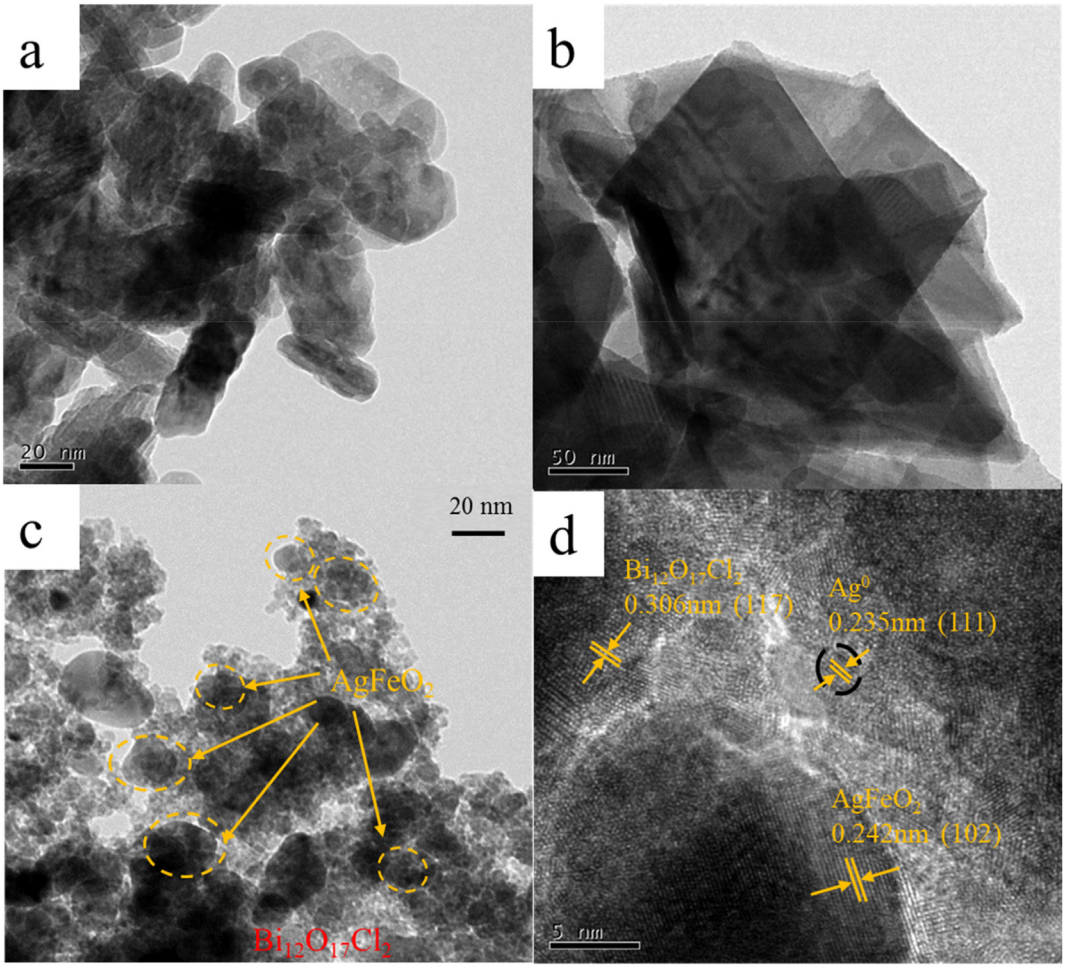

Fig. 3. (a–c) TEM images of $AgFeO_2$, $Bi_{12}O_{17}Cl_2$ and 20-BAF, respectively; (d) HRTEM image of 20-BAF.

region owing to surface plasmon resonance (SPR) effect induced by Ag NPs and the formation of Z-scheme heterojunction (Liang et al., 2011; Zhou et al., 2011). Moreover, the optical band gap energies could be calculated according to the following Eq. (5):

$$\alpha h\nu = A(h\nu - Eg)^{n/2} \quad (5)$$

where α, h, ν, Eg, and A are the absorption coefficient, Planck's constant, light frequency, band gap energy, and a constant, respectively. The n value of AFO is 1 for direct transition, which is 4 for BOC for the indirect transition (Zhou et al., 2018b; Chen et al., 2019). According to the plots (Fig. 4b) of $(\alpha h\nu)^2$ ($(\alpha h\nu)^{1/2}$) *versus* ($h\nu$), the band gap values of AFO and BOC were determined to be 1.85 and 2.23 eV, respectively.

The separation and transfer efficiency of photoexcited carriers were also assessed. Fig. 4c displayed the transient photocurrent curve of pure AFO, pure BOC, AF, 20-BF and 20-BAF. The intensity of photocurrent responses under the same experimental condition exhibited the following order: 20-BAF > 20-BF > BOC > AF > AFO. This phenomenon demonstrated that the presence of Ag nanoparticles played positive role in the separation of photogenerated electron-hole pairs. Besides, the charge migration efficiency was evaluated by EIS analysis. As can be seen from Fig. 4d, the arc radius of 20-BAF was smaller than that of single AFO and BOC, even smaller than that of AF and 20-BF, indicating that 20-BAF composite exhibited the lower electron transfer resistance. The experimental EIS data were then fitted to the equivalent circuit using Zview software for a better understanding of the EIS measurement results. As exhibited in Fig. 4d (inset), their R_{ct} values was calculated as ~ 18314, 12153, and 1989 ohmega for the AFO sample, BOC sample, and 20-BAF sample, respectively. It reflects that the charge transfer resistance of 20-BAF is reduced by 89% and 84% compared to AFO and BOC, respectively, which further verifies that 20-BAF exhibits more efficient interfacial charge-carrier transfer. Furthermore, the surface recombination constants of AFO, BOC and 20-BAF were investigated by the decay profile of OCP. The average recombination constant was determined by equation: $(E - Ep)/(Ed - Ep) = 1 - \exp^{-kt}$ (Li et al., 2020). E represents OCP at any time, Ep represents photo-stationary OCP value, and Ed represents OCP stationary value in the dark environment, and k denotes the pseudo-first order recombination rate constant (s^{-1}). As presented in Figs. 4e and 20-BAF possessed a slower transient OCP curve compared with the AFO and BOC monomers. Specifically, the surface recombination constant of 20-BAF was calculated to be 0.0031 s^{-1}, which was 2.5 and 1.6 times smaller than AFO (0.0077 s^{-1}) and BOC (0.0049 s^{-1}) respectively, which further proves that the construction of Z-scheme heterojunction can hinder the surface recombination of photogenerated carriers.

It can be concluded from the above analysis that the optical absorption capacity, the lifetime of photoexcited carriers and the separation and transfer efficiency of photogenerated electron-hole pairs are improved significantly by constructing heterojunction

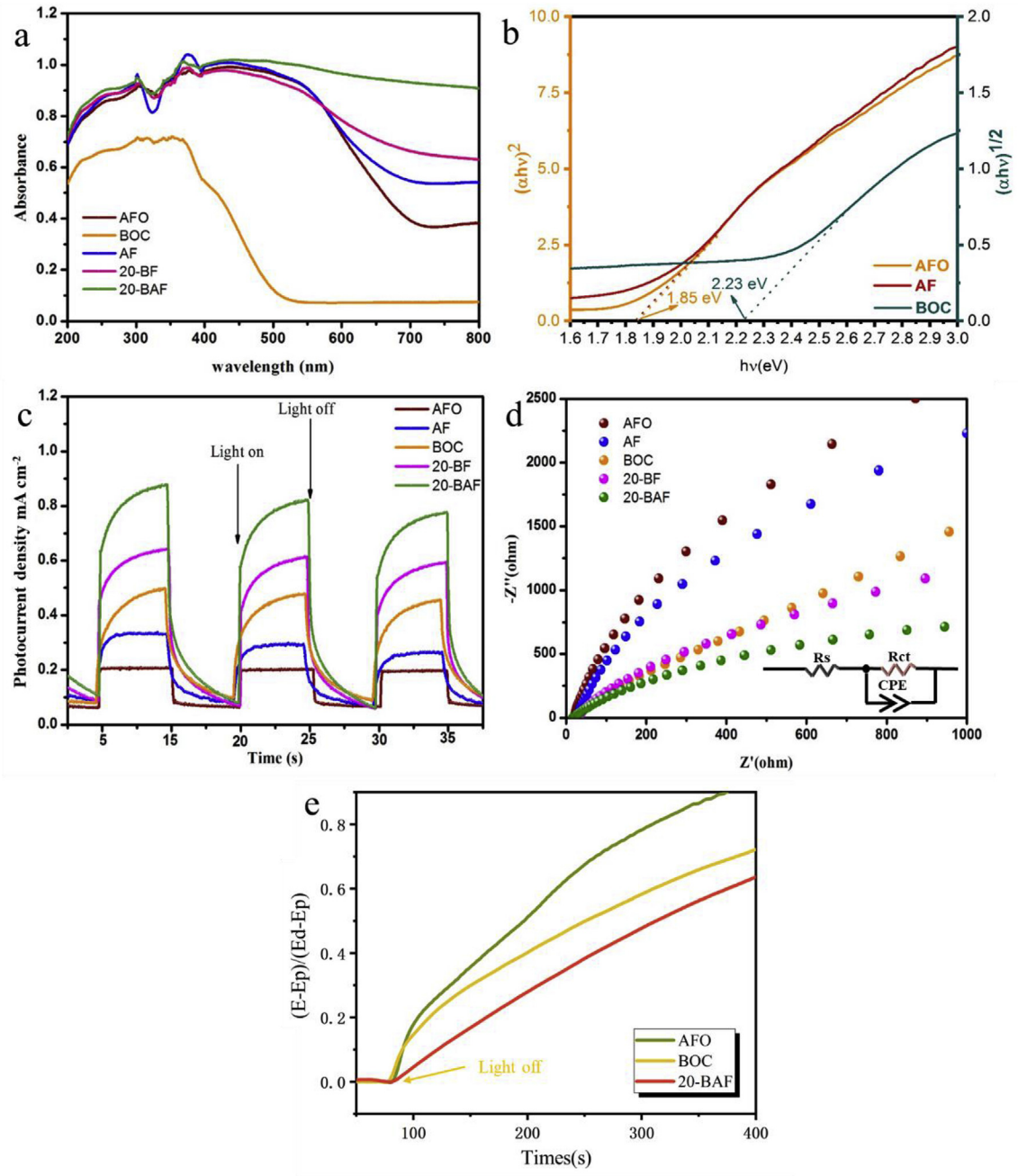

Fig. 4. (a) UV–vis adsorption spectra of AFO, BOC, AF, 20-BF,and 20-BAF samples, (b) Plots of $(\alpha h\nu)^2$ vs photon energy ($h\nu$) for AFO and AF, plots of $(\alpha h\nu)^{1/2}$ vs photon energy ($h\nu$) for BOC, (c)Transient photocurrent responses of pure AFO, BOC, AF, 20-BF and 20-BAF, (d) EIS Nyquist plots of pure AFO, BOC, AF, 20-BF and 20-BAF under visible light irradiation together with an equivalent circuit (inset). Rs, solution resistance; Rct, electron-transfer resistance; CPE, constant phase element, (e) Normalized open-circuit potential (OCP) decay curves after turning off the visible light (n > 420 nm).

between AFO and BOC as well as the introducing of Ag nanoparticles, which are expected for enhancing the photodegradation performance.

3.1.3. Specific surface area analysis

Nitrogen adsorption and desorption isotherms, which combined with BET and BJH analysis methods can obtain the specific surface area and pore size distribution of the samples, is an important test method for characterizing the structure of materials. The nitrogen absorption-desorption isotherms (Fig. SM-2a) of the synthesized samples (AFO, AF, 20-BF, 20-BAF) matched well with typical IUPAS IV-type pattern with sharp inflection of nitrogen adsorbed volume at high P/P_0 about 0.9 (type H3 hysteresis loop), demonstrating the existence of mesoporous structure in these samples. In addition, the corresponding pore size distribution measurements (Fig. SM-2b) verified that their mesoporous structure had a narrow average pores diameter slightly larger than 2 nm. Besides, the particular characterization results were exhibited in Table SM-1. Compared with pure AFO (28.75 $m^2\ g^{-1}$, $\sigma = 1.311$), the BET surface areas of the AF (33.55 $m^2\ g^{-1}$, $\sigma = 0.407$), 20-BF (52.76 $m^2\ g^{-1}$, $\sigma = 0.774$) and 20-BAF (69.50 $m^2\ g^{-1}$, $\sigma = 0.845$) are significantly enhanced, and σ stands for standard deviation. The relatively high BET surface area of 20-BAF mainly attributed to that BOC nanosheets played an excellent role in inhibiting the self-agglomeration

of AFO, offering more active sites on surface exposed to TC molecules. According to the above results, abundant active sites and mesoporous structure (He et al., 2015) of the 20-BAF composite contributed to the improvement of photocatalytic performance.

3.2. Photocatalytic degradation of TC

3.2.1. Photocatalytic activity of the prepared catalysts

The photocatalytic performance of as-prepared catalysts (AFO, BOC, AF, 20-BF and BAF composites) was investigated by degrading TC. Undergo adsorption-desorption equilibrium within 1 h dark reaction, all samples were exposed to visible light. It can be seen from Fig. 5a that the removal efficiencies of the AFO, BOC, AF, 20-BF, 10-BAF, 15-BAF, 20-BAF, and 25-BAF were 46.8%, 53.9%, 62.0%, 77.3%, 87.6%, 91.9%, 94.1%, and 89.6%, respectively. Obviously, among all the BAF composites, 20-BAF presented the best performance for the TC removal with an efficiency of 94.1% in 1h under visible light illumination. Excessive content of BOC would further reduce the crystallinity of AFO, thereby inhibiting the photocatalytic activity (Wang et al., 2016). Therefore, the photocatalytic activity of 25-BAF was decreased, which indicated that the proper amount of BOC was crucial. Moreover, 20-BAF had a good adsorption capacity for TC in darkness due to the enhanced BET surface areas offering abundant active sites, which was beneficial for the removal of TC. To shed light on the quantitative characterization of TC photocatalytic degradation kinetics, the experimental data were linear fitted by $\ln(C_0/C_t) = kt$, where C_0, C_t and k represent the concentration of TC at the adsorption−desorption equilibrium, the TC concentration after visible light irradiation and the slope of the corresponding fitting curves, respectively. The k denotes the degradation rate constant can reflect the photocatalytic ability of these as-prepared samples under visible light illumination. As shown in Fig. 5b, the degradation rate of AF was higher than AFO, which indicated that the loading of Ag^0 helped to increase the photocatalytic activity of AFO. Besides, degradation rate constant of 20-BF was higher than that of AFO and BOC which proved that the formation of heterojunction contributed to the improvement of photocatalytic performance. The 20-BAF composite showed the highest degradation rate for TC, which was 2.4, 3.7, 3.3 and 6.5 times higher than those of the 20-BF, AF, BOC and AFO, respectively. Besides, a comparison of photocatalytic activity of 20-BAF with other photocatalysts was exhibited in Table SM-2, which revealed that 20-BAF has relatively excellent performance for the degradation of 40 mg L^{-1} TC under visible light illumination. Furthermore, leaching concentration of metal ions in the treated solution is exhibited in Table SM-3, which reflected that when tetracycline in the solution is effectively degraded by 20-BAF, the concentration of heavy metal ions separated from 20-BAF met the World Health Organization standard, which would not cause secondary pollution to the solution. Therefore, construction of heterojunctions and the loading of Ag^0 not only facilitated the separation of electron-hole pairs but also distinctly heightened the capacity of visible light absorption, thereby contributing to the photocatalytic performance enhancement of 20-BAF.

3.2.2. Influence factors of TC removal

The influence of photocatalysts concentration, pH value, anions species, and humic acid (HA) concentration on the degradation of TC were studied with the aim of making 20-BAF composites meet the actual wastewater treatment.

Various concentrations (0.1, 0.25, 0.5, 0.75 and 1 g L^{-1}) of the photocatalyst were participated in the degradation of TC. As shown in Fig. SM-3a, when the concentration of the 20-BAF composites increased from 0.1 to 0.5 g L^{-1}, the degradation efficiency obviously enhanced to 87.4% from 13.4% under 60 min visible light illumination. The enhanced photocatalytic performance was mainly due to the increase of photocatalysts providing more active sites to generate strongly oxidized radicals for the degradation of TC. However, further increased the catalyst concentration from 0.5 to 1 g L^{-1}, the TC removal rate was slightly reduced. The results implied that an excessive concentration of the photocatalyst led to the enhancement of solution turbidity (Table SM-4) and agglomeration of catalyst thereby resulting in negative effects on TC degradation (Xu et al., 2018a). Hence, 0.5 g L^{-1} was the best catalyst concentration for removal of TC (40 mg L^{-1}), on the basis of balancing the cost and removal efficiency of the photocatalyst.

It is well known that the pH value of the solution can affect the stability and the surface charge of the catalyst as well as tetracycline speciation through the protonation-deprotonation reaction and thus affects the photocatalytic activity. The TC molecules can form three molecular species in solution, including cationic species (pH < 3.3), zwitterionic species (3.3 < pH < 7.68) and anionic species (pH > 7.68) (Wang et al., 2018a). 20-BAF exhibited different surface charge properties at different pH conditions which was displayed in Table SM-5. Therefore, the mutual adsorption between TC molecular and 20-BAF surface was affected by the pH of the solution thereby affecting the photocatalytic effect. Fig. SM-3b exhibited the removal efficiency of TC by 20-BAF at pH = 2, 3.8

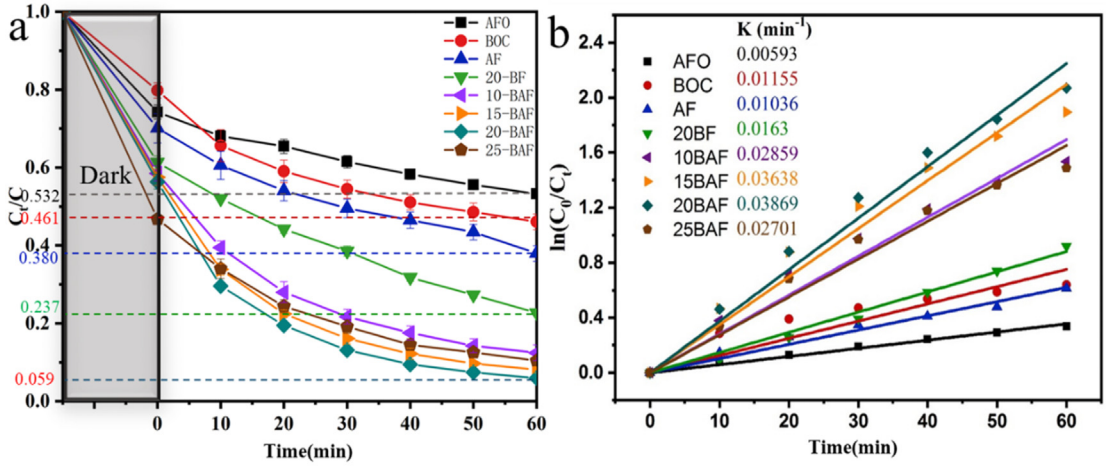

Fig. 5. (a) Photocatalytic degradation of TC under visible light illumination; (b) pseudo-first-order reaction kinetics.

(control, without pH adjustment with HCl or NaOH), 5, 7, 9. When the solution pH = 9, the degradation rate of TC was only 36%. This poor removal effect was mainly due to the repulsive force between the anionic species of TC and negatively charged 20-BAF composites. This meant that the adsorption of tetracycline molecules on the surface 20-BAF was the premise of TC degradation. The degradation efficiencies of TC increase with decreasing pH value from 7 to 3.8. At this pH range, tetracycline molecules existed as zwitterionic species, and 20-BF composites were positively charged. Thus, the changes in TC degradation was not caused by Coulombic force. As shown in Table SM-5, the zeta potential of 20-BAF increased as the pH decreases suggesting that it had better dispersion in low pH solution, thus TC solution had the best removal efficiency at pH = 3.8. This implies that excellent dispersibility played a positive part in the degradation process of contaminants. However, when the pH value dropped to 2, the strong acid environment caused the decomposition of 20-BAF ($FeO_2^- + 4H^+ \rightarrow Fe^{3+} + 2H_2O$) resulting in the sharp decrease in the degradation efficiency. The above analysis showed that both weakly acidic and neutral conditions is suitable for the degradation of TC by 20-BAF, that is, the slight fluctuation of pH would not significantly affect the photocatalytic performance of 20-BAF, which made it practically applicable.

Since natural water and contaminated water commonly contain inorganic anions (CO_3^{2-}, SO_4^{2-} and NO_3^-), it is essential to systematically assess the effect of their existence on the TC degradation. Na_2CO_3, Na_2SO_4 and $NaNO_3$ (10 mM) were adopted to investigate the effects of coexisting anions. As can be seen in Fig. SM-3c, CO_3^{2-} displayed suppressive effects on the photodegradation of TC in two aspects: First, the addition of Na_2CO_3 increased the pH of the solution, which was detrimental to TC degradation (Fig. SM-3b). Second, CO_3^{2-} and its hydrolysate HCO_3^- (Eq. (6)) are generally considered as effective hydroxyl radical (•OH) scavenger ($k_{\bullet OH/CO_3^{2-}} = 3.9 \times 10^8\ M^{-1}\ S^{-1}$ and $k_{\bullet OH/HCO_3^-} = 8.5 \times 10^6\ M^{-1}\ S^{-1}$) (Eqs. (7) and (8)) (Ao et al., 2019). Besides, the produced $CO_3^{\bullet-}$ is generally regard as less reactive radicals compared to •OH (Senobari and Nezamzadeh-Ejhieh, 2018). Thus, CO_3^{2-} played negative roles in photocatalytic degradation TC process. In addition, the presence of SO_4^{2-} was also adverse to the photodegradation of TC owning to the capture of photoinduced holes by SO_4^{2-} (Xue et al., 2018). The inhibitory effect on TC of SO_4^{2-} was also reported by Zhu et al. (2014). Furthermore, the hole scavenging effect of NO_3^- (Eq. (9)) also adversely affected the degradation of TC (Hua et al., 2014; Parrino et al., 2018). The involved reactions occurred as follows:

$$CO_3^{2-} + H_2O \rightarrow OH^- + HCO_3^- \quad (6)$$

$$HCO_3^- + \bullet OH \rightarrow CO_3^{\bullet-} + H_2O \quad (7)$$

$$CO_3^{2-} + \bullet OH \rightarrow CO_3^{\bullet-} + OH^- \quad (8)$$

$$NO_3^- + h^+ \rightarrow NO_3 \quad (9)$$

In real effluents, tetracyclines usually coexist with natural dissolved organics. Humic acid (HA) is a typical dissolved organic substance whose rich functional groups affect the photodegradation process. Fig. SM-3d illustrated that the appearance of HA inhibited the degradation of TC, and higher concentrations of HA exhibited stronger inhibitory effects. The following two reasons might account for this phenomenon: (i) light shielding effect of HA: due to the dark color of humic acid and some insoluble particles, it would affect the incident light reaching the surface of the photocatalyst (Liu et al., 2018); (ii) scavenging effect of HA on reactive oxygen species: HA can act as ·OH sink, which subsequently decreased the degradation efficiency of TC (Wang et al., 2018a). The similar inhibitory effect of HA was also performed on the photodegradation of hydroperfluorocarboxylic acids (Liu et al., 2018).

3.2.3. Reusability and possible degradation pathway

The stability of the photocatalyst is important indicators for its application to actual water treatment. Therefore, photocatalytic activity for six consecutive cycles was investigated and the XRD patterns before and after the degradation experiments were compared to assess the stability of the optimal 20-BAF. As seen in Fig. SM-4a, the photocatalytic effect of 20-BAF was relatively stable in the first five applications. The removal efficiency of the fifth time was still 81%, which insinuated the superior recyclability of the photocatalyst. However, in the sixth use, the removal efficiency was significantly reduced, only 70%. Therefore, we think that it is better not to use 20-BAF more than 5 times. Simultaneously, XRD patterns (Fig. SM-4b) illustrated that the main component of 20-BAF remain unchanged, although the peaks of BOC and Ag became more obvious which resulted from the photoreduction of AFO on the surface of 20-BAF. At the same time, it could be concluded that the photoreduction of AFO was the main reason for the decline in photocatalytic performance after five cycles of experiments. Furthermore, Fig. SM-4c showed that the morphology of 20-BAF did not change significantly after visible light illumination, which further confirmed the superior recyclability of 20-BAF.

In order to go deep into the photocatalytic degradation routes of TC over 20-BAF composites, LC-MS technique was adopted to precisely detect the reaction intermediates formed in the photocatalytic degradation process, and the MS spectra were presented in Fig. SM-5. As shown in Fig. SM-5, only the main peak with m/z = 445.1 was identified, which was assigned to the TC molecule, indicating that no decomposition or deterioration of TC was produced before illumination. With the increasing of illumination time, the peak intensity of TC gradually decreased and some new peaks of intermediates appeared obviously (Fig. SM-5b-f). The intermediate products in accordance with the charge-to-mass ratio were analyzed, and probable degradation pathways of TC were elaborated in Fig. 6. In this work, the degradation intermediate products proposed were not completely consistent with the results of previous reports, which might be determined by the unique characteristic of 20-BAF.

Firstly, 20-BAF composites with high specific surface area and abundant micropores adsorb a large number of TC molecules (m/z = 445.1). After reaching the adsorption-desorption equilibrium, the TC solution contained 20-BAF composites were exposed toward visible light to produce rich $\cdot O_2^-$, h^+ and ·OH instantly. The active species ($\bullet O_2^-$, h^+ and •OH) excited in the photocatalytic system would attack the double bonds, aromatic ring and amino group in the TC degradation process, it meant that all the intermediates were mainly produced by the ring-opening reactions or the cleavage of the main carbon bond (He et al., 2014). Under contact with $\bullet O_2^-$ and •OH, P1 with m/z value of 459 was generated via addition of hydroxyl. Previous studies regarding theoretical formation of TC degradation products in solution indicated that the double bond at the C_{11a}–C_{12} position of TC was the most reactive site for oxidants to attack, and a rearrangement with the hydroxyl at the position C_{12} would lead to the generation of P1 (Chen et al., 2017). The molecular ion of m/z 459 has also been detected in previous work of Chen et al. (2019). Then, P2 (m/z = 433) is generated by N-dealkylation of the C_4 tertiary amine site due to the low N-C bond energy (Chen et al., 2017). Subsequently, the hydroxyl group at the C_6 position of P2 might be attacked by active species. C_6 is the most likely site for dehydration, which could lead to the formation of a stable second aromatic ring C due to the tautomerization of C_{11a} –C_{12} keto-enol (Liu et al., 2016). Then the electron-

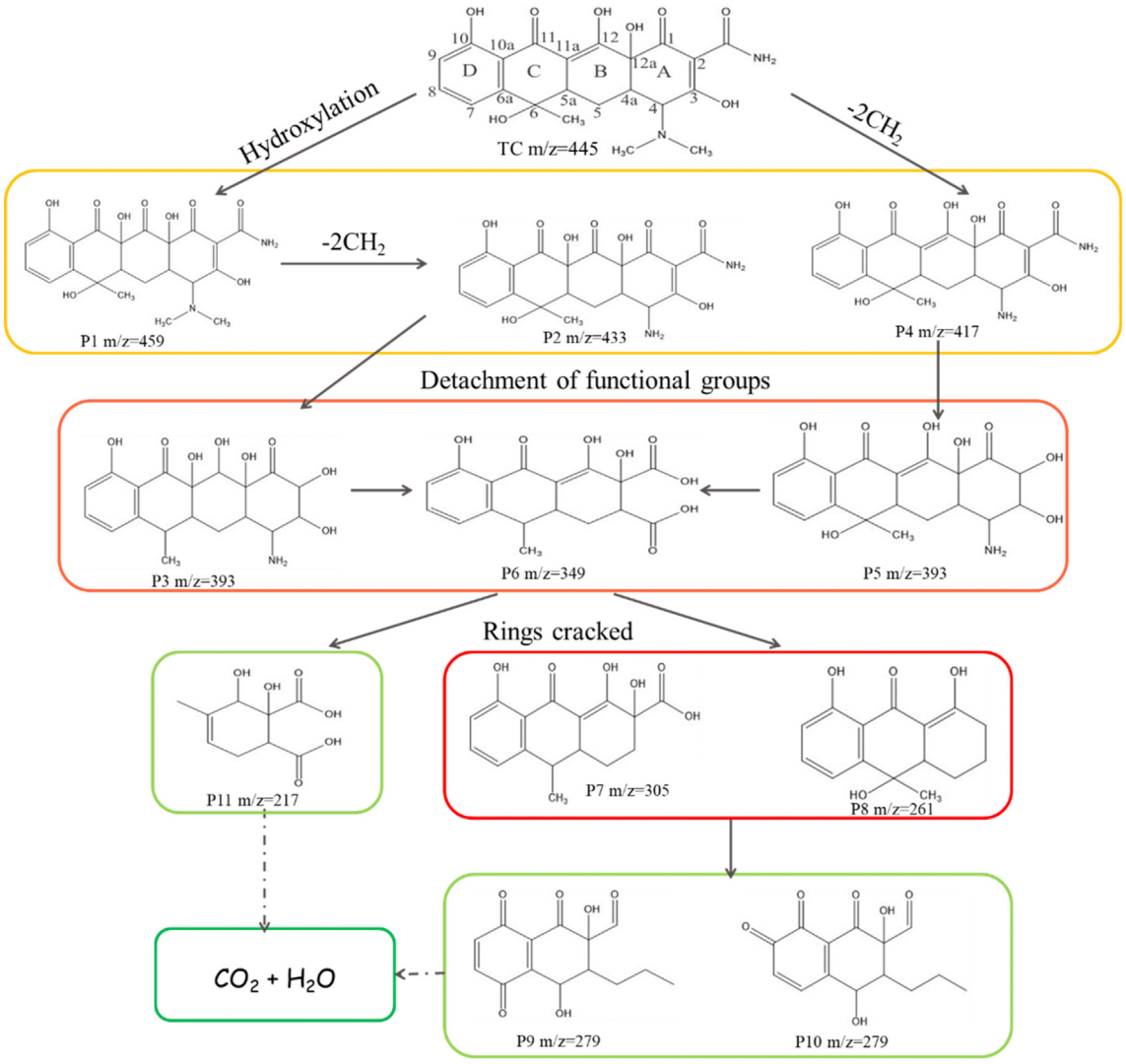

Fig. 6. Possible TC photodegradation pathway over 20-BAF.

rich double C_2-C_3 is easily attacked by •OH to generated P3 (m/z = 393) (Wang et al., 2020a). In another pathway, TC molecular firstly experiences N-dealkylation to generate P4 (m/z = 417) via mechanisms similar to that involved in the P2. Then •OH attacked electron-rich double C_2-C_3 to form P5 (m/z = 417). P3 and P5 could further transform during photocatalytic oxidation to formation P6 (m/z = 349) via cleavage of the carboatomic ring A. The similar mechanism of action was introduced in the generation of molecular ion with an m/z value of 333 in the work investigated by Chen et al. (2017). Afterwards, decarboxylation reaction occurs to form P7 and P8 (Chen et al., 2017). Then, a ketone at C_7 or C_9 is produced by the attack of active radicals at the ortho (C_9) or para (C_7) positions of the phenolic ring, and resulting in the difference in molecular structure between P9 and P10. Simultaneously, active radicals attack C_{11a}-C_{12} double bond which is a reactive site leading to the formation of P9 and P10. The similar formation process of molecular ions of m/z 279 has also been reported in previous work of Wang et al. (2020a). Besides, the generation of P11 is stem from the cleavage of double-bond in aromatic ring B of P6 (He et al., 2014). Eventually, these photoinduced intermediates can all be decomposed to carbon dioxide and water under the continues attack of active species.

3.3. Possible photocatalysis mechanism

When semiconductors with staggered band structure are in contact to form heterojunction, it is necessary to examine the charge transfer mode in the photocatalytic reaction. Usually, radical trapping experiment is a powerful method to analyze charge transfer pathway by the maintained strong redox ability of photogenerated carriers. Because Z-scheme transfer pathway can preserve and utilize the redox ability with more negative conduction band potential and more positive valence band potential, it has sufficient redox ability to produce reactive oxygen species when the type-II transfer mode fails to provide the required redox capacity (Tang et al., 2020). Besides, some researchers believed that Fermi level difference between two semiconductor photocatalysts is the pre-requisite for inducing charge redistribution and the formation of internal electric field, which significantly affect the photogenerated charge carrier separation and transfer process (Xu et al., 2018b; Chen et al., 2019). Thus, in our work, we firstly determine the band structures and Fermi levels of each component of BOC/Ag/AFO to analyze its preferred photocatalytic mechanism, and then verify its mechanism through free radical capture experiments, and ESR technology.

Firstly, the valence band (VB) and conduction band (CB)

positions of AFO and BOC was firstly determined to investigate photocatalytic mechanism. The flat band potential of AFO and BOC were calculated via Mott−Schottky plots (Fig. SM-6). Mott-Schottky plots is a primary method for determining flat band potentials (Cooper, 1982). The positive slope of the linear $1/C^2$ potential curves illustrated that both AFO and BOC equipped the typical n-type semiconductor characteristics (Yan et al., 2017). Simultaneously, the flat band potential of AFO and BOC were calculated to be 0.05 and −0.94 V versus Ag/AgCl electrode (SCE), respectively. Thus, they were 0.29 and −0.7 V versus normal hydrogen electrode (NHE). Furthermore, the flat band potential of an n-type semiconductor is more positive than that of CB, about 0.1. Hence, the CB potential of AFO and BOC were determined to be 0.19 and −0.8 V vs. NHE, respectively. In addition, the band gaps of AFO and BOC were calculated to be 1.85 and 2.23 V, respectively (Fig. 4b). Consequently, the VB positions of AFO and BOC were 2.04 and 1.43 V, respectively.

Besides, Fermi level difference between two semiconductor photocatalysts is the pre-requisite for inducing charge redistribution and the formation of internal electric field, which significantly affects the photogenerated charge carrier separation and transfer process (Xu et al., 2018b; Chen et al., 2019). In our study, the components of $Bi_{12}O_{17}Cl_2$/Ag/$AgFeO_2$ had matched Fermi energy levels leading to the form of built-in electric fields between $Bi_{12}O_{17}Cl_2$ and Ag and between Ag and $AgFeO_2$ with the same electric field direction, which favored carrier migration followed the Z-scheme pathway. Specifically, the Fermi level for the n-type semiconductor is equal to the flat potential (Tian et al., 2017). So, the Fermi levels of AFO and BOC were 0.29 and −0.7 V vs. NHE, respectively. Besides, the Fermi level of metal Ag was 0.14 V (vs. NHE)(Shi et al., 2019). When the metal and n-type semiconductors were in contact, the difference of Fermi levels would lead to the transfer of free electrons between metals and semiconductor (Zhang and Yates, 2012). Therefore, electrons would flow from BOC to Ag^0 until the Fermi levels of metal and semiconductor were aligned, causing the forming of electric field (represented by red E in Fig. 7) and the upward bending of energy bands of BOC (Zhang and Yates, 2012). Similarly, electric field in the same direction would form between Ag and AFO, and the energy bands of AFO would bend downward. Consequently, when the ternary AFO/Ag/BOC system was under visible light illumination, photoinduced holes in BOC and photoinduced electron in AFO would transfer to metal Ag under the influence of the built-in electric field (represented by red E in Fig. 7) and achieved recombination finally (Li et al., 2016), which was the preferred charge transfer mode under the influence of the built-in electric field. The existence of built-in electric field favored the recombination between the photogenerated electrons in the CB of AFO and photogenerated holes in the VB of BOC. Photocatalytic AFO/Ag/BOC system with such carriers' transfer pathway is considered as Z-scheme system.

Furthermore, radical trapping experiments was performed to verify the above conjecture. The results of radical trapping experiments (Fig. SM-7a-b) showed that after the addition of benzoquinone (BQ, a typical superoxide radical scavenger) only 11.1% of TC was degraded which can infer that $\bullet O_2^-$ played dominated roles during TC degradation. However, if a conventional heterojunction was constructed between AFO, Ag and BOC (the upper side of Fig. 7), electrons would assembled in the CB of AFO which did not have sufficient reductive ability to generate $\bullet O_2^-$, as CB potential (0.19 V) of AFO was less negative than the redox potential of $O_2/\bullet O_2^-$ (−0.033 V vs NHE) (Chen et al., 2019). Therefore, only when the photoexcited electrons migrate according to the Z-scheme pathway (the down side of Fig. 7), can they have sufficient reductive ability to generate enough superoxide radicals to play a predominant role in the degradation of TC. Besides, ESR technology also clearly detected the generation of superoxide radicals under visible light illumination (Fig. SM-7c), which further supported the above results. Besides, the hydroxyl radicals (Fig. SM-9d) generated in the photocatalytic system were stem from the reaction of $\bullet O_2^-$ radicals on the CB of BOC with H^+ rather than hole oxidation because the VB edge potential of AFO (2.023 V) was less positive than that of $OH^-/\bullet OH$ (+2.4 V vs NHE).

Based on the above experimental results and analysis, the photocatalytic reaction mechanism for the 20-BAF was proposed and exhibited in the down side of Fig. 7. Under the illumination of visible light, narrow band gap semiconductors AFO and BOC were induced to produce photoexcited electron-hole pairs. Then, electrons in the CB of AFO shifted to electron-shuttle mediators (Ag nanoparticles), followed by recombination with the equivalent holes generated on the VB of BOC. As a result, the electrons in the CB of BOC could be retain to reduce the absorbed oxygen to produce reactive $\bullet O_2^-$ which could further react with surface absorbed H^+ to generate $\bullet OH$ radicals or directly oxidize TC molecules. Meanwhile, the photogenerated holes with high oxidizing abilities in the VB of AFO could effectively play a part in the degradation process of TC molecules. Moreover, after Ag nanoparticles were introduced into the photocatalytic system, the light absorption ability of photocatalysts, the surface electron stimulation as well as the interfacial electron migration were boosted (Yuan et al., 2017). All of the above related reactions were summarized as follows:

$$AgFeO_2 + h\nu \rightarrow AgFeO_2\ (h^+/e^-) \quad (10)$$

$$Bi_{12}O_{17}Cl_2 + h\nu \rightarrow Bi_{12}O_{17}Cl_2\ (h^+/e^-) \quad (11)$$

$$Ag^0 + h\nu \rightarrow Ag^0\ (e^-)\ (SPR) \quad (12)$$

$$e^-(BOC) + O_2 \rightarrow \bullet O_2^- \quad (13)$$

$$\bullet O_2^-(BOC) + H^+ \rightarrow \bullet OH \quad (14)$$

$$h^+/\bullet OH\ /\bullet O_2^- + TC \rightarrow \text{degraded products} \quad (15)$$

Overall, the formation of Z-scheme heterojunction which not only promoted the separation and transfer of the photogenerated charge carriers, but also retained the strong reduction and oxidation capability. In addition, the SPR effect of Ag nanoparticles could enhance light absorption ability and broaden the light absorption range to the whole visible light. Therefore, 20-BAF possessed the significantly improved photocatalytic activity for TC removal.

4. Conclusions

In conclusion, a series of $Bi_{12}O_{17}Cl_2$/Ag/$AgFeO_2$ Z-scheme photocatalysts were successfully synthesized and characterized. The optimal $Bi_{12}O_{17}Cl_2$/Ag/$AgFeO_2$ composites with 20 wt% $Bi_{12}O_{17}Cl_2$ decoration (20-BAF) presented the best photocatalytic performance towards TC degradation, with a removal efficiency of 94.1% after dark processing and 1 h visible light illumination. In addition, an optimum catalyst concentration of 0.5 g L^{-1} and a primeval pH (without adjustment) favored the degradation process, while the introduction of exogenous anions (CO_3^{2-}, SO_4^{2-} and NO_3^-) and organic matter (HA) supressed the degradation of TC. Furthermore, The excellent stability and reusability of the 20-BAF Z-scheme system were verified over six cycles of the photodegradation reactions and a possible degradation pathway for TC was proposed based on the identified degradation products. Finally, the enhancement of photocatalytic performance in the 20-BAF Z-scheme system was mainly attributed to the following three aspects: (i) the decoration of Ag nanoparticles extended the optical

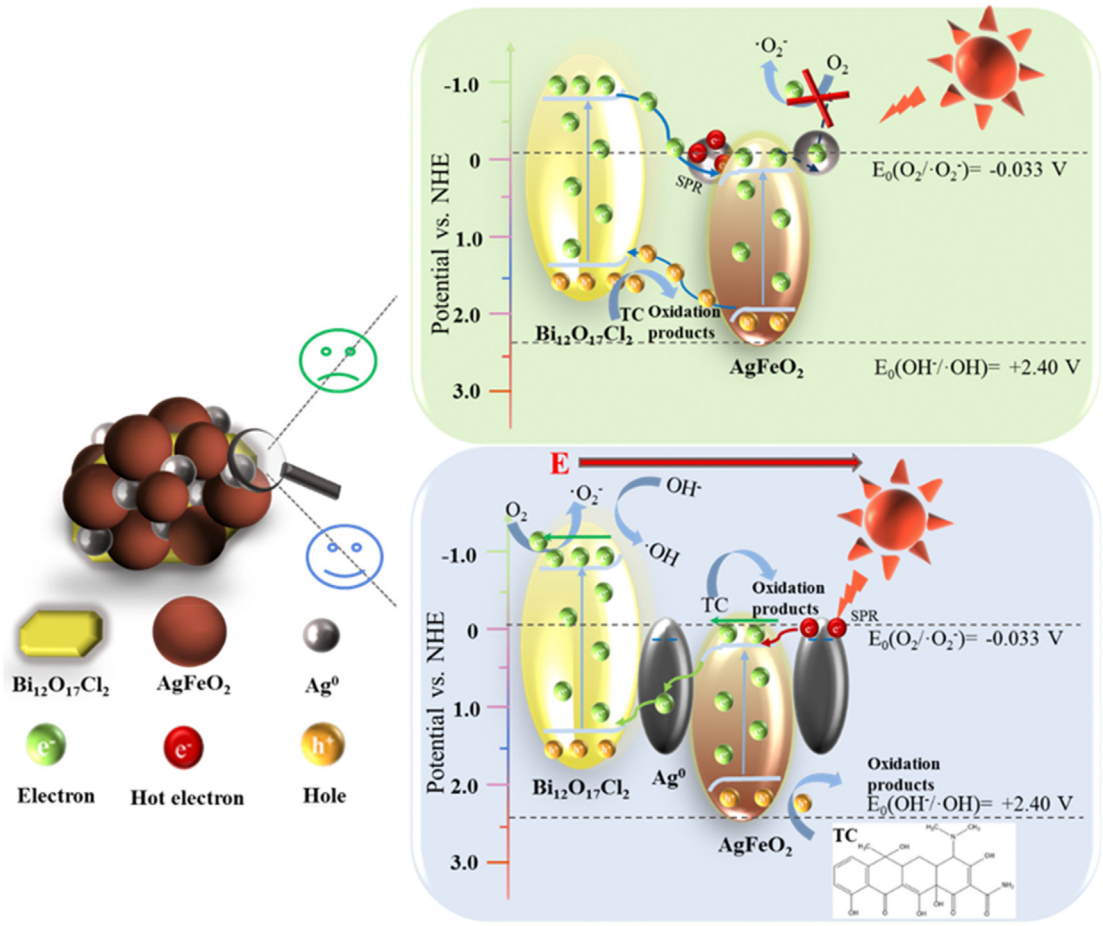

Fig. 7. Possible photocatalytic TC degradation mechanism under visible light illumination over 20-BAF composites.

response range and enhanced the light absorption ability; (ii) 2D $Bi_{12}O_{17}Cl_2$ nanosheets as substrates efficaciously suppressed the aggregation of $AgFeO_2$ nanoparticles achieving increased specific surface area to provide more adsorption active sites for TC molecules, which promoted the efficient use of photogenerated carriers and active radicals; (iii) The formation of Z-scheme system promoted the separation of photogenerated carriers and the utilization of the powerful electrons and holes.

Credit author statement

Jiayin Guo: Conceptualization, Methodology, Investigation, Formal analysis, Writing - original draft. Longbo Jiang: Methodology, Formal analysis, Validation, Writing - Review & Editing. Jie Liang: Supervision, Funding acquisition. Weihua Xu: Writing - review & editing, Formal analysis. Hanbo Yu: Investigation, Writing - review & editing, Formal analysis. Jin Zhang: Writing - review & editing, Formal analysis. Shujing Ye: Writing - review & editing, Formal analysis. Wenle Xing: Writing - review & editing. Xingzhong Yuan: Supervision, Writing - review & editing.

Declaration of competing interest

The authors declare that they have no known competing financial interests or personal relationships that could have appeared to influence the work reported in this paper.

Acknowledgement

This work was supported by the National Natural Science Foundation of China (51979101, 51739004, 51679082, 51521006), the Hunan Science & Technology Innovation Program (2018RS3037), the Natural Science Foundation of Hunan Province (2019JJ20002) and Science and Technology Plan Project of Hunan Province (No. 2018SK2047), the Fundamental Research Funds for the Central Universities (531118010394).

Appendix A. Supplementary data

Supplementary data to this article can be found online at https://doi.org/10.1016/j.chemosphere.2020.128651.

References

Anandan, S., Ashokkumar, M., 2009. Sonochemical synthesis of Au-TiO_2 nanoparticles for the sonophotocatalytic degradation of organic pollutants in aqueous environment. Ultrason. Sonochem. 16, 316–320.

Ao, X.W., Sun, W.J., Li, S.M., Yang, C., Li, C., Lu, Z.D., 2019. Degradation of tetracycline by medium pressure UV-activated peroxymonosulfate process: influencing factors, degradation pathways, and toxicity evaluation. Chem. Eng. J. 361, 1053–1062.

Bu, Y.Y., Chen, Z.Y., Sun, C.J., 2015. Highly efficient Z-Scheme Ag_3PO_4/Ag/WO_3-- photocatalyst for its enhanced photocatalytic performance. Appl. Catal. B Environ. 179, 363–371.

Chang, F., Luo, J.R., Wang, X.F., Xie, Y.C., Deng, B.Q., Hu, X.F., 2015. Poly(vinyl pyrrolidone)-assisted hydrothermal synthesis and enhanced visible-light photocatalytic performance of oxygen-rich bismuth oxychlorides. J. Colloid Interface Sci. 459, 136–145.

Chen, Y.Y., Ma, Y.L., Yang, J., Wang, L.Q., Lv, J.M., Ren, C.J., 2017. Aqueous tetracycline degradation by H_2O_2 alone: removal and transformation pathway. Chem. Eng. J. 307, 15–23.
Chen, S., Huang, D.L., Zeng, G.M., Gong, X.M., Xue, W.J., Li, J., Yang, Y.Y., Zhou, C.Y., Li, Z.H., Yan, X.L., Li, T., Zhang, Q., 2019. Modifying delafossite silver ferrite with polyaniline: visible-light-response Z-scheme heterojunction with charge transfer driven by internal electric field. Chem. Eng. J. 370, 1087–1100.
Cooper, G., Turner, J.A., Nozik, A.J., 1982. Mott-Schottky plots and flatband potentials for single crystal rutile electrodes. J. Electrochem. Soc. 129, 1973–1977.
El-Bassuony, A.A.H., Abdelsalam, H.K., 2018. Synthesis, characterization and antimicrobial activity of $AgFeO_2$ delafossite. J. Mater. Sci. Mater. Electron. 29, 11699–11711.
Greiner, M.T., Helander, M.G., Tang, W.M., Wang, Z.B., Qiu, J., Lu, Z.H., 2011. Universal energy-level alignment of molecules on metal oxides. Nat. Mater. 11, 76–81.
Guo, J.Y., Liang, J., Yuan, X.Z., Jiang, L.B., Zeng, G.M., Yu, H.B., Zhang, J., 2018. Efficient visible-light driven photocatalyst, silver (meta)vanadate: synthesis, morphology and modification. Chem. Eng. J. 352, 782–802.
He, D., Sun, Y.B., Xin, L., Feng, J.W., 2014. Aqueous tetracycline degradation by non-thermal plasma combined with nano-TiO_2. Chem. Eng. J. 258, 18–25.
He, F., Chen, G., Zhou, Y.S., Yu, Y.G., Zheng, Y., Hao, S., 2015. The facile synthesis of mesoporous g-C_3N_4 with highly enhanced photocatalytic H_2 evolution performance. Chem. Commun. 51, 16244–16246.
Hua, Y.J., Chen, G.L., Xu, X.N., Zou, X.M., Liu, J.Y., Wang, B., Zhao, Z.M., Chen, Y., Wang, C.T., Liu, X.Y., 2014. Comparative study of homogeneous and heterogeneous photocatalytic degradation of RhB under visible light irradiation with Keggin-type manganese-substituted catalysts. J. Phys. Chem. C 118, 8877–8884.
Huang, D.L., Chen, S., Zeng, G.M., Gong, X.M., Zhou, C.Y., Cheng, M., Xue, W.J., Yan, X.L., Li, J., 2019. Artificial Z-scheme photocatalytic system: what have been done and where to go? Coord. Chem. Rev. 385, 44–80.
Jiang, L.B., Yuan, X.Z., Zeng, G.M., Liang, J., Wu, Z.B., Wang, H., Zhang, J., Xiong, T., Li, H., 2018. A facile band alignment of polymeric carbon nitride isotype heterojunctions for enhanced photocatalytic tetracycline degradation. Environ. Sci.: Nano 5, 2604–2617.
Kashyap, J., Riaz, U., 2018. Facile synthesis of novel polypyrrole dispersed $AgFeO_2$ nanohybrid with highly efficient photocatalytic activity towards 2,4,6-trichlorophenol degradation. RSC Adv. 8, 13218–13225.
Li, S., Zhao, Q.D., Wang, D.J., Xie, T.F., 2016. Work function engineering derived all-solid-state Z-scheme semiconductor-metal-semiconductor system towards high-efficiency photocatalytic H_2 evolution. RSC Adv. 6, 66783–66787.
Li, B.S., Liu, S.Y., Lai, C., Zeng, G.M., Zhang, M.M., Zhou, M.Z., Huang, D.L., Qin, L., Liu, X.G., Li, Z.W., An, N., Xu, F.H., Yi, H., Zhang, Y.J., Chen, L., 2020. Unravelling the interfacial charge migration pathway at atomic level in 2D/2D interfacial Schottky heterojunction for visible-light-driven molecular oxygen activation. Appl. Catal. B Environ. 266, 118650.
Liang, Y.C., Wang, C.C., Kei, C.C., Hsueh, Y.C., Cho, W.H., Perng, T.P., 2011. Photocatalysis of Ag-Loaded TiO_2 nanotube arrays formed by atomic layer deposition. J. Phys. Chem. C 115, 9498–9502.
Liu, Y.Q., He, X.X., Fu, Y.S., Dionysiou, D.D., 2016. Kinetics and mechanism investigation on the destruction of oxytetracycline by UV-254nm activation of persulfate. J. Hazard Mater. 305, 229–239.
Liu, J.Q., Li, C.G., Qu, R.J., Wang, L.H., Feng, J.F., Wang, Z.Y., 2018. Kinetics and mechanism insights into the photodegradation of hydroperfluorocarboxylic acids in aqueous solution. Chem. Eng. J. 348, 644–652.
Ouyang, S.X., Kikugawa, N., Chen, D., Zou, Z.G., Ye, J.H., 2009. A systematical study on photocatalytic properties of $AgMO_2$ (M = Al, Ga, In): effects of chemical compositions, crystal structures, and electronic structures. J. Phys. Chem. C 113, 1560–1566.
Parrino, F., Livraghi, S., Giamello, E., Palmisano, L., 2018. The existence of nitrate radicals in irradiated TiO_2 aqueous suspensions in the presence of nitrate ions. Angew. Chem. Int. Ed. 57, 10702–10706.
Ray, S.K., Dhakal, D., Gyawali, G., Joshi, B., Koirala, A.R., Lee, S.W., 2019. Transformation of tetracycline in water during degradation by visible light driven Ag nanoparticles decorated α-$NiMoO_4$ nanorods: mechanism and pathways. Chem. Eng. J. 373, 259–274.
Senobari, S., Nezamzadeh-Ejhieh, A., 2018. A p-n junction NiO-CdS nanoparticles with enhanced photocatalytic activity: a response surface methodology study. J. Mol. Liq. 257, 173–183.
Shi, H.X., Wang, C.J., Zhao, Y.Y., Liu, E.Z., Fan, J., Ji, Z., 2019. Highly efficient visible light driven photocatalytic inactivation of E. coli with Ag QDs decorated Z-scheme $Bi_2S_3/SnIn_4S_8$ composite. Appl. Catal. B Environ. 254, 403–413.
Song, Z., He, Y.Q., 2017. Novel AgCl/Ag/$AgFeO_2$ Z-scheme heterostructure photocatalyst with enhanced photocatalytic and stability under visible light. Appl. Surf. Sci. 420, 911–918.
Sun, H.B., Qin, P.F., Wu, Z.B., Liao, C.J., Guo, J.Y., Luo, S., Chai, Y.Z., 2020. Visible light-driven photocatalytic degradation of organic pollutants by a novel Ag_3VO_4/Ag_2CO_3 p–n heterojunction photocatalyst: mechanistic insight and degradation pathways. J. Alloys Compd. 834, 155211.
Tang, D.D., Zhang, G.K., 2017a. Fabrication of $AgFeO_2$/g-C_3N_4 nanocatalyst with enhanced and stable photocatalytic performance. Appl. Surf. Sci. 391, 415–422.
Tang, D.D., Zhang, G.K., 2017b. Ultrasonic-assistant fabrication of cocoon-like Ag/$AgFeO_2$ nanocatalyst with excellent plasmon enhanced visible-light photocatalytic activity. Ultrason. Sonochem. 37, 208–215.
Tang, Q.Y., Chen, W.F., Lv, Y.R., Yang, S.Y., Xu, Y.H., 2020. Z-scheme hierarchical Cu_2S/Bi_2WO_6 composites for improved photocatalytic activity of glyphosate degradation under visible light irradiation. Separ. Purif. Technol. 236, 116243.
Tian, N., Zhang, Y.H., Li, X.W., Xiao, K., Du, X., Dong, F., Waterhouse, G.I.N., Zhang, T.R., Huang, H.W., 2017. Precursor-reforming protocol to 3D mesoporous g-C_3N_4 established by ultrathin self-doped nanosheets for superior hydrogen evolution. Nanomater. Energy 38, 72–81.
Wang, Y., Zhang, H., Zhang, J.H., Lu, C., Huang, Q.Q., Wu, J., Liu, F., 2011. Degradation of tetracycline in aqueous media by ozonation in an internal loop-lift reactor. J. Hazard Mater. 192, 35–43.
Wang, J.H., Shen, Y.F., Li, Y., Liu, S.Q., Zhang, Y.J., 2016. Crystallinity modulation of layered carbon nitride for enhanced photocatalytic activities. Chemistry 22, 12449–12454.
Wang, H., Wu, Y., Feng, M.B., Tu, W.G., Xiao, T., Xiong, T., Ang, H.X., Yuan, X.Z., Chew, J.W., 2018a. Visible-light-driven removal of tetracycline antibiotics and reclamation of hydrogen energy from natural water matrices and wastewater by polymeric carbon nitride foam. Water Res. 144, 215–225.
Wang, W.J., Xu, P., Chen, M., Zeng, G.M., Zhang, C., Zhou, C.Y., Yang, Y., Huang, D.L., Lai, C., Cheng, M., Hu, L., Xiong, W.P., Guo, H., Zhou, M., 2018b. Alkali metal-assisted synthesis of graphite carbon nitride with tunable band-gap for enhanced visible-light-driven photocatalytic performance. ACS Sustain. Chem. Eng. 6, 15503–15516.
Wang, W.J., Zeng, Z.T., Zeng, G.M., Zhang, C., Xiao, R., Zhou, C.Y., Xiong, W.P., Yang, Y., Lei, L., Liu, Y., Huang, D.L., Cheng, M., Yang, Y.Y., Fu, Y.K., Luo, H.Z., Zhou, Y., 2019. Sulfur doped carbon quantum dots loaded hollow tubular g-C_3N_4 as novel photocatalyst for destruction of Escherichia coli and tetracycline degradation under visible light. Chem. Eng. J. 378, 122132.
Wang, H.L., Chen, T.H., Chen, D., Zou, X.H., Li, M.X., Huang, F.J., Sun, F.W., Wang, C., Shu, D.B., Liu, H.B., 2020a. Sulfurized oolitic hematite as a heterogeneous Fenton-like catalyst for tetracycline antibiotic degradation. Appl. Catal. B Environ. 260, 118203.
Wang, L., Min, X.P., Sui, X.Y., Chen, J.H., Wang, Y., 2020b. Facile construction of novel $BiOBr/Bi_{12}O_{17}Cl_2$ heterojunction composites with enhanced photocatalytic performance. J. Colloid Interface Sci. 560, 21–33.
Xing, W.L., Liang, J., Tang, W.W., He, D., Yan, M., Wang, X.X., Luo, Y., Tang, N., Huang, M., 2020. Versatile applications of capacitive deionization (CDI)-based technologies. Desalination 482, 114390.
Xu, L., Yang, L., Johansson, E.M.J., Wang, Y.H., Jin, P.K., 2018a. Photocatalytic activity and mechanism of bisphenol a removal over TiO_2−x/rGO nanocomposite driven by visible light. Chem. Eng. J. 350, 1043–1055.
Xu, Q.L., Zhang, L.Y., Yu, J.G., Wageh, S., Al-Ghamdi, A.A., Jaroniec, M., 2018b. Direct Z-scheme photocatalysts: principles, synthesis, and applications. Mater. Today 21, 1042–1063.
Xue, Y., Wang, P.F., Wang, C., Ao, Y.H., 2018. Efficient degradation of atrazine by BiOBr/UiO-66 composite photocatalyst under visible light irradiation: environmental factors, mechanisms and degradation pathways. Chemosphere 203, 497–505.
Yamashita, T., Hayes, P., 2008. Analysis of XPS spectra of Fe^{2+} and Fe^{3+} ions in oxide materials. Appl. Surf. Sci. 254, 2441–2449.
Yan, M., Hua, Y.Q., Zhu, F.F., Gu, W., Jiang, J.H., Shen, H.Q., Shi, W.D., 2017. Fabrication of nitrogen doped graphene quantum dots-BiOI/$MnNb_2O_6$ p-n junction photocatalysts with enhanced visible light efficiency in photocatalytic degradation of antibiotics. Appl. Catal. B Environ. 202, 518–527.
Ye, S.J., Yan, M., Tan, X.F., Liang, J., Zeng, G.M., Wu, H.P., Song, B., Zhou, C.Y., Yang, Y., Wang, H., 2019. Facile assembled biochar-based nanocomposite with improved graphitization for efficient photocatalytic activity driven by visible light. Appl. Catal. B Environ. 250, 78–88.
Yin, L., Shi, Y.B., Lu, L., Fang, R.Y., Wan, X.K., Shi, H.X., 2016. A novel delafossite structured visible-light sensitive $AgFeO_2$ photocatalyst: preparation, photocatalytic properties, and reaction mechanism. Catalysts 6, 69.
Yu, H.B., Jiang, L.B., Wang, H., Huang, B.B., Yuan, X.Z., Huang, J.H., Zhang, J., Zeng, G.M., 2019. Modulation of Bi_2MoO_6-based materials for photocatalytic water splitting and environmental application: a critical review. Small 15, 1901008.
Yuan, X.Z., Jiang, L.B., Chen, X.H., Leng, L.J., Wang, H., Wu, Z.B., Xiong, T., Liang, J., Zeng, G.M., 2017. Highly efficient visible-light-induced photoactivity of Z-scheme $Ag_2CO_3/Ag/WO_3$ photocatalysts for organic pollutant degradation. Environ. Sci.: Nano 4, 2175–2185.
Zeng, Y., Guo, N., Li, H.Y., Wang, Q.Y., Xu, X.J., Yu, Y., Han, X.R., Yu, H.W., 2019. Construction of flower-like MoS_2/Ag_2S/Ag Z-scheme photocatalysts with enhanced visible-light photocatalytic activity for water purification. Sci. Total Environ. 659, 20–32.
Zhang, Z., Yates Jr., J.T., 2012. Band bending in semiconductors: chemical and physical consequences at surfaces and interfaces. Chem. Rev. 112, 5520–5551.
Zhang, Q.Q., Ying, G.G., Pan, C.G., YS, Liu, Y.S., Zhao, J.L., 2015. Comprehensive evaluation of antibiotics emission and fate in the river basins of China: source analysis, multimedia modeling, and linkage to bacterial resistance. Environ. Sci. Technol. 49, 6772–6782.
Zhou, B., Zhao, X., Liu, H.J., Qu, J.H., Huang, C.P., 2011. Synthesis of visible-light sensitive M–$BiVO_4$ (M=Ag, Co, and Ni) for the photocatalytic degradation of

organic pollutants. Separ. Purif. Technol. 77, 275–282.
Zhou, C.Y., Lai, C., Xu, P., Zeng, G.M., Huang, D.L., Zhang, C., Cheng, M., Hu, L., Wan, J., Liu, Y., Xiong, W.P., Deng, Y.C., Wen, M., 2018b. In situ grown AgI/$Bi_{12}O_{17}Cl_2$ heterojunction photocatalysts for visible light degradation of sulfamethazine: efficiency, pathway, and mechanism. ACS Sustain. Chem. Eng. 6, 4174–4184.
Zhou, C.Y., Lai, C., Xu, P., Zeng, G.M., Huang, D.L., Li, Z.H., Zhang, C., Cheng, M., Hu, L., Wan, J., Chen, F., Xiong, W.P., Deng, R., 2018a. Rational design of carbon-doped carbon nitride/$Bi_{12}O_{17}Cl_2$ composites: a promising candidate photocatalyst for boosting visible-light-driven photocatalytic degradation of tetracycline. ACS Sustain. Chem. Eng. 6, 6941–6949.
Zhu, X.D., Wang, Y.J., Zhou, D.M., 2014. TiO_2 photocatalytic degradation of tetracycline as affected by a series of environmental factors. J. Soils Sediments 14, 1350–1358.